

# Supporting information

## Wearable, Luminescent Oxygen Sensor for Transcutaneous Oxygen Monitoring

*Chang-Jin Lim<sup>†,§</sup>, Soyeon Lee<sup>†,§</sup>, Jin-Hoon Kim<sup>†</sup>, Hye-Jun Kil<sup>‡</sup>, Yu-Chan Kim<sup>‡</sup>, and Jin-Woo Park<sup>\*,†</sup>*

<sup>†</sup>Department of Materials Science and Engineering, Yonsei University, Seoul, 03722, Korea

<sup>‡</sup>Biomedical Research Institute, Korea Institute of Science and Technology, Seoul, 02792, Korea

<sup>§</sup> These authors contributed equally to this work

<sup>\*</sup>Corresponding author at: 213 Engineering Hall 2, Yonsei University, Seoul, 03722, Korea

E-mail address: jwpark09@yonsei.ac.kr (Jin-Woo Park)

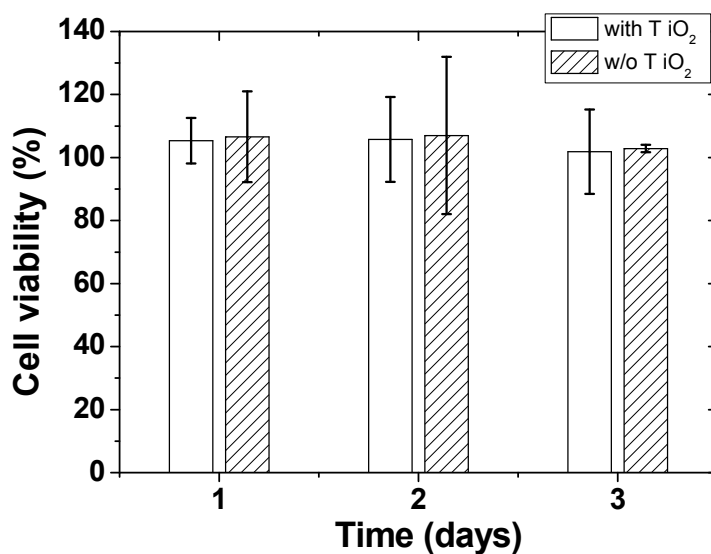


**Figure. S1** L929 fibroblast viability after direct seeding on the TiO<sub>2</sub>-doped sensing film and sensing film w/o TiO<sub>2</sub> (n = 3).

Cell viability was assessed using the Cell Counting Kit 8 (CCK-8, Dojindo, Japan) to determine whether the surface of the TiO<sub>2</sub>-doped sensing film or the sensing film w/o TiO<sub>2</sub> is toxic when attached onto human skin. Compared to the control, on which the cells grew well, both the TiO<sub>2</sub>-doped sensing film and the sensing film w/o TiO<sub>2</sub> showed a cell viability of over 80%, indicating that the sensing films do not act as irritants to human skin.

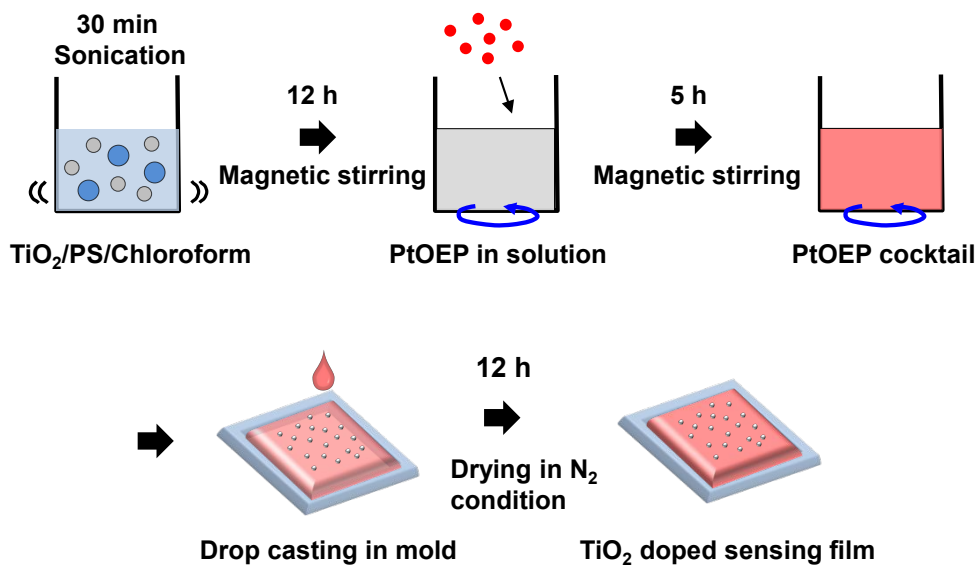


**Figure. S2** Schematic of the sensing film fabrication process.

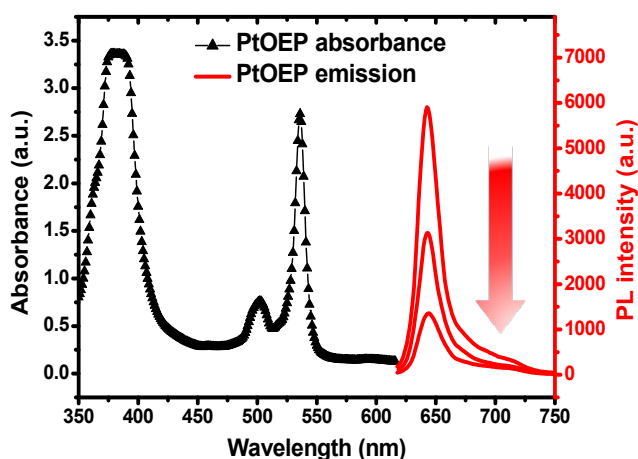


**Figure. S3** PtOEP absorption and emission spectra.

The PtOEP absorption spectrum consists of two peaks called the Soret band (390 nm) and the Q band (500-550 nm), while the single emission peak of PtOEP is at 645 nm. We utilized Q band for our system not Soret band, since it is cost ineffective and complex to make OLED or LED with Soret band range and PtOEP can absorb enough Q band range light. The PL of

PtOEP at 645 nm is quenched by  $O_2$  molecules, resulting in decreased intensity with increasing  $[O_2]$ .

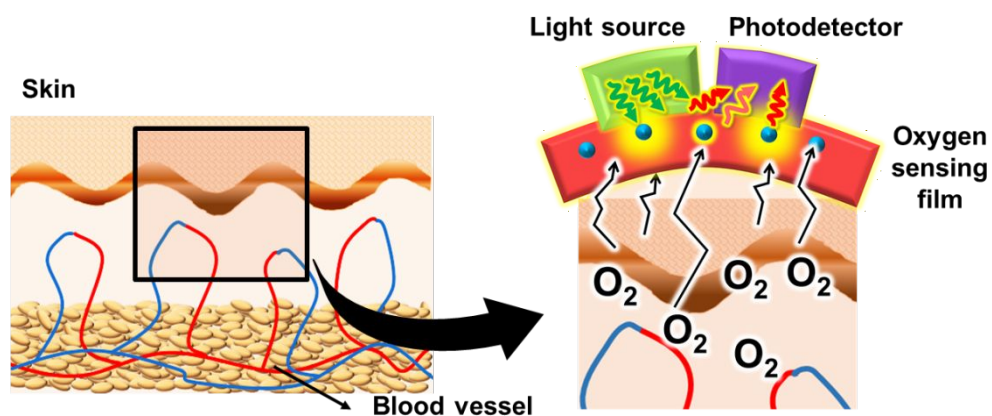


**Figure. S4** Schematics of the working mechanisms in the bandage-type  $O_2$  sensor receiving the  $O_2$  molecules diffused out from the blood vessels.

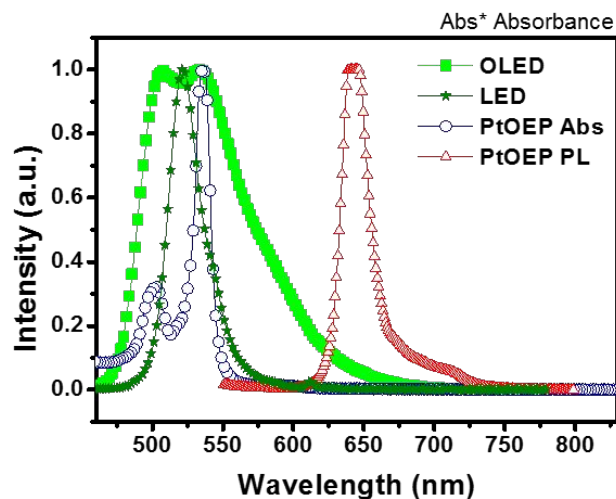
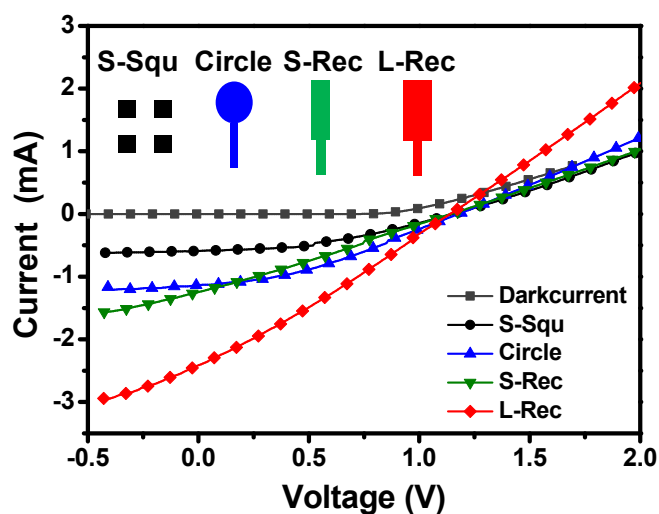


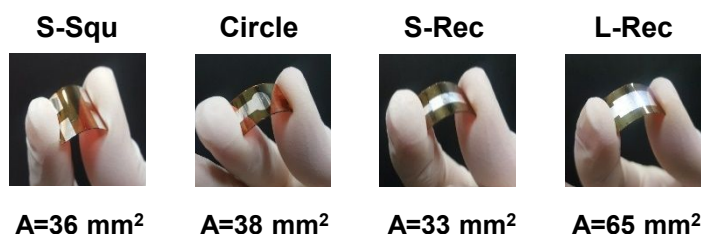
**Figure. S5** Comparison between EL spectra of green OLED, LED and absorption and PL emission spectra of sensing film.

The full width half maximum (FWHM) of OLED is much larger than that of LED, due to the disordered polymer chains in organic system, which is hardly observed in crystalline inorganic system.<sup>1</sup> These broad EL spectrum of OLED is not a problem for sensing film absorbing light, since the EL of OLED sufficiently covers the absorption spectrum of sensing film. However, the EL tail of OLED extends over the wavelength of 600 nm region, which is hardly distinguishable from the PL of the sensing film. Therefore, the sensitivity of sensor with OLED will be lower than that with LED, even though an optical filter effectively filtered below the wavelength of 620 nm.

(a)

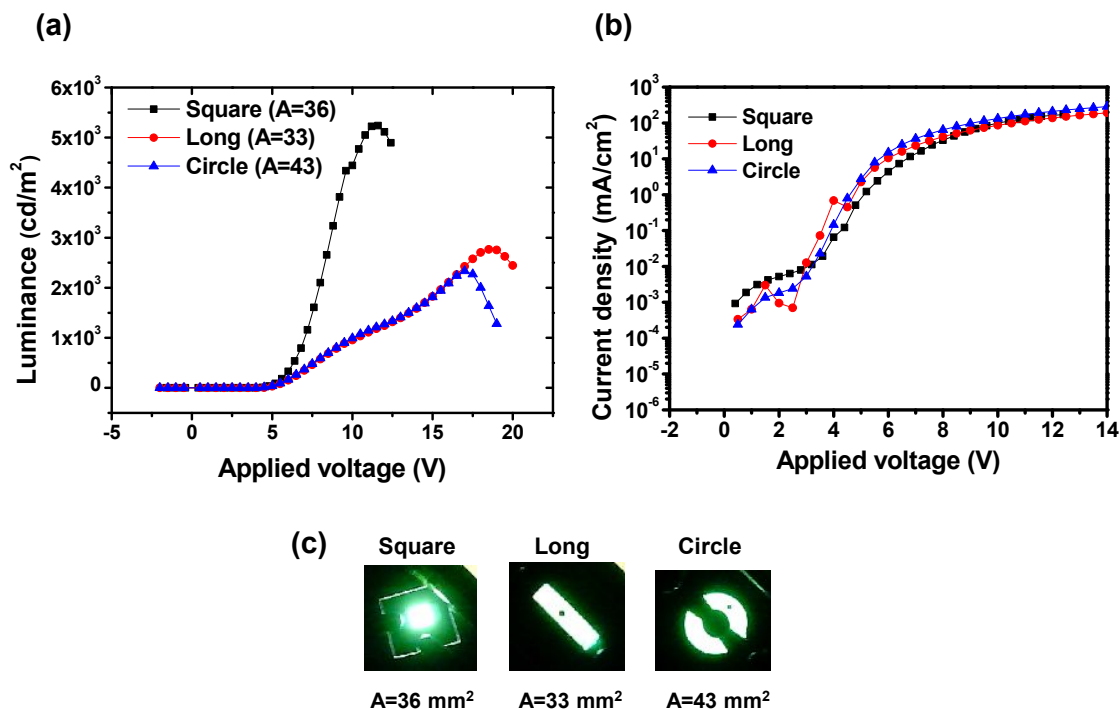


(b)



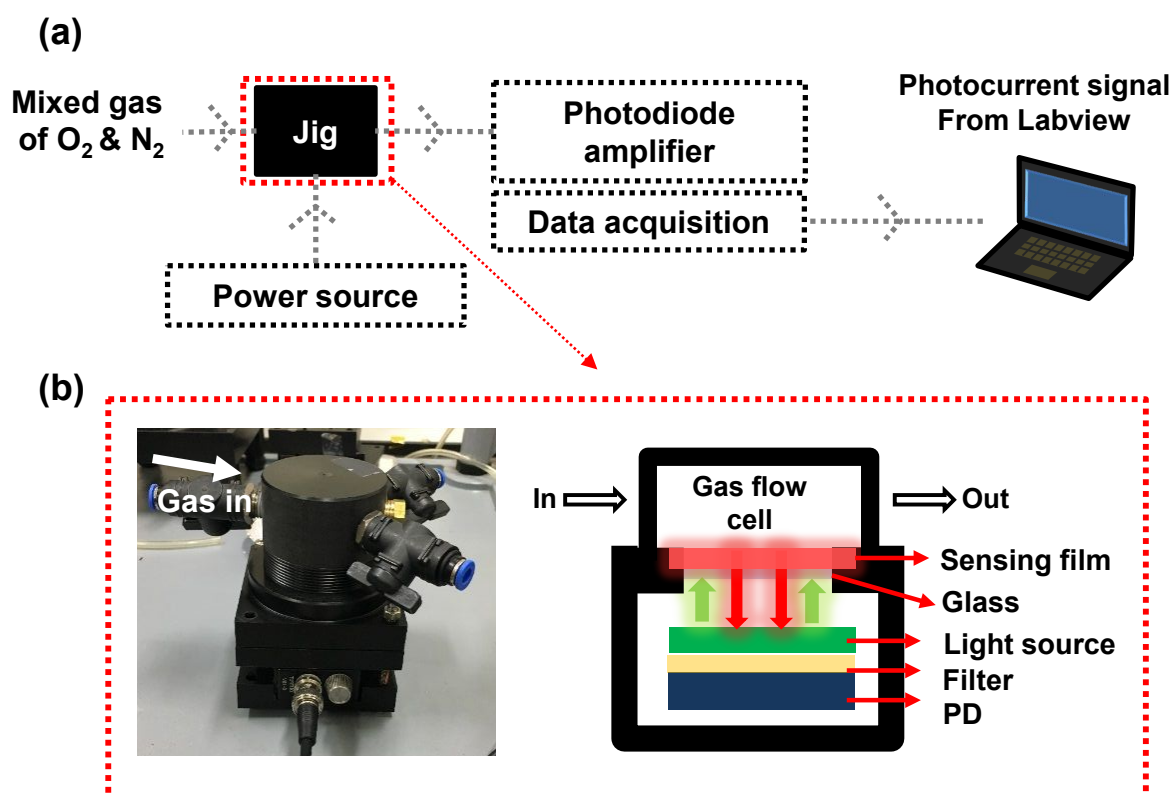
**Figure. S6** (a) OPD  $I$ - $V$  characteristics in relation to the shape of the Al cathode. (b) Digital photographs of the flexible OPD with various Al cathode shapes (S-squ, Circle, S-Rec and L-Rec type OPD images with the corresponding active area of the device ( $A = \text{mm}^2$ )).

Figure. S6a shows the  $I$ - $V$  characteristics of the OPD in relation to the Al cathode shape. Optimizing the size of the OPD active area (which is the same as the area covered by the Al cathode) can minimize the loss of detected light coming from the PL sensing film since the light from the sensing film is emitted in random directions.<sup>2</sup> As shown in the graph, the current generated from the OPD with a large rectangular Al cathode (L-Rec) was highest among the other types of OPDs presented in Figure. S6a. Hence, the L-Rec OPD showed the highest  $I_{\text{light}}/I_{\text{dark}}$  ratio among all the type of OPDs prepared in this work considering that there was no significant difference in their dark current.



**Figure. S7** (a)  $L$ - $V$  and (b)  $J$ - $V$  characteristics of the OLEDs with varying shapes. (c) Digital photographs of the OLEDs at the applied  $V$  of 7 V for the Square OLED and 14 V for both the Long and Circle OLEDs with an active area of 36, 33, and 43 mm<sup>2</sup>, respectively.

The larger active area of the OLED generally induces reduced efficiency and nonuniform lighting or hot spots, among others.<sup>3</sup> Therefore, as shown in Figure. S7a, the  $L_{\max}$  and  $L$ - $V$  slope are smaller for the Long and Circle OLEDs than the Square OLED, and the  $J$ - $V$  characteristics show a similar behavior (Figure. S7b). Considering the operating  $V$  and  $L$  of the OLEDs, we decided to use the Square OLED for the integration. The large area of illumination of the sensing film could be achieved by linking four Square OLEDs in a parallel circuit, thus lighting up four OLEDs at the same time.



**Figure. S8** (a) Schematics of the measurement set up and (b) digital photograph of the jig.

As shown in Figure. S8a, the photocurrent and  $I_0/I_{30}$  of the sensing film were obtained using an in-house measurement setup. A mixture of O<sub>2</sub> and N<sub>2</sub> gas was injected into the measurement jig. The sensing film comes in contact with the gas mixture while being excited by the light source (Figure. S8b). An optical filter is placed on the PD in order to minimize the background noise from light with wavelengths outside the emission peak of the PtOEP in the sensing film. The photocurrent generated from the PD is amplified through a photodiode amplifier and then transferred to a data acquisition module for data streaming via a LabVIEW program.



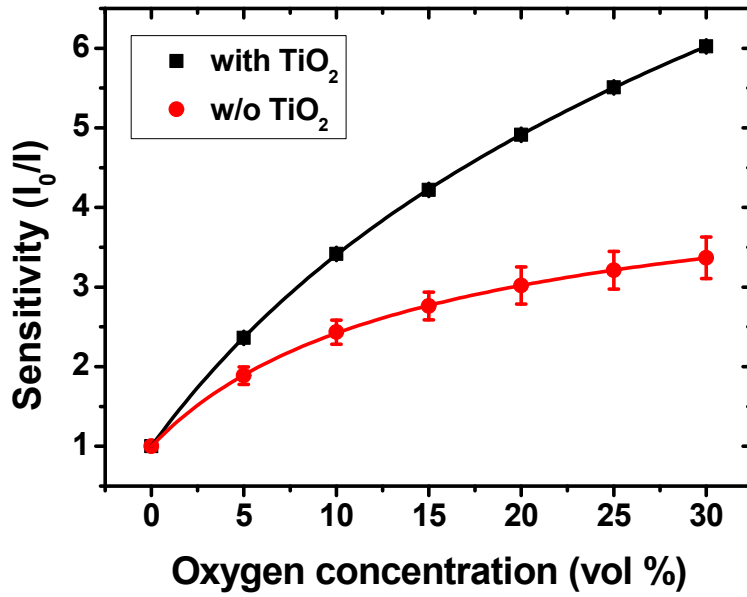


**Figure. S9** Stern–Volmer plot of the  $\text{TiO}_2$  NP-doped sensing film and sensing film w/o  $\text{TiO}_2$ .

The curves in Figure. S9 were fitted using the two-site model equation described as

$$\frac{I_0}{I} = \left( \frac{f_1}{1 + K_{sv}^1 [O_2]} + \frac{f_2}{1 + K_{sv}^2 [O_2]} \right)^{-1} \quad (2)$$

where  $I_0$  and  $I$  are the intensities of the PL from the  $\text{O}_2$  sensing film in the absence and presence of  $\text{O}_2$ , respectively,  $K_{sv}^1$  and  $K_{sv}^2$  are the Stern–Volmer constants,  $f_1$  and  $f_2$  are the fractions of the  $\text{O}_2$  molecules uniformly and nonuniformly in contact with the PtOEP dye molecules, respectively ( $f_1 + f_2 = 1$ ), and  $[O_2]$  is the  $\text{O}_2$  concentration. As described in Table 1, the  $I_0/I_{30}$  of the sensing film was enhanced from 3.2 to 6 by using  $\text{TiO}_2$  NPs in the sensing film to act as light-scattering centers.

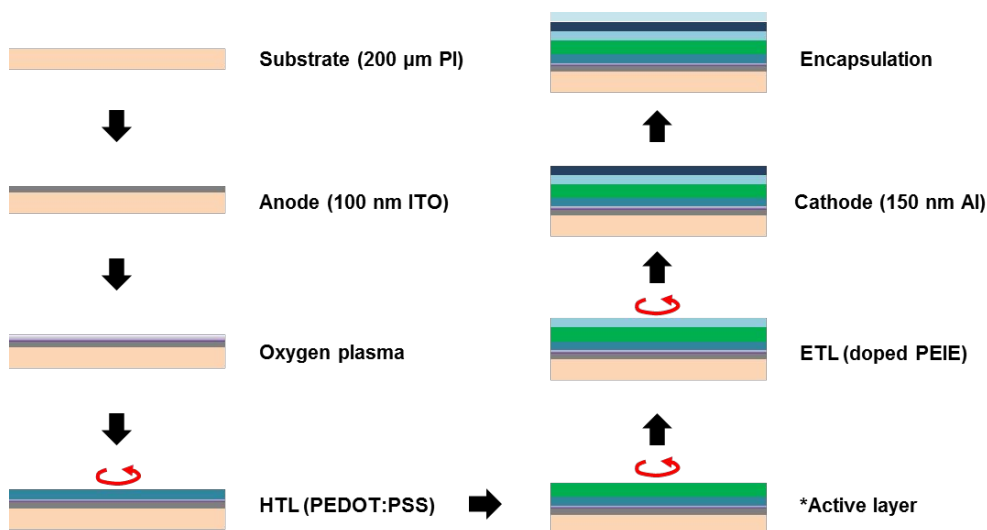


**Figure. S10** Schematic of the OPD and OLED fabrication processes. (\*Active layer: Polymer green in OLED and P3HT:PCBM in OPD)

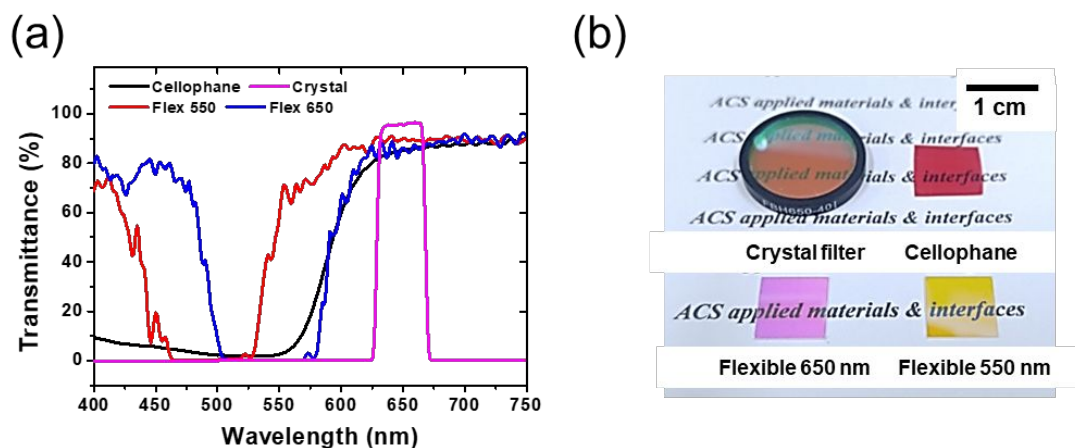


**Figure. S11** (a) The transmittance spectra and (b) digital photographs of the different kinds of optical filters (crystal, cellophane and two types of flexible filters).

Four kinds of optical filters were tested in this work. The four optical filters were

categorized as crystal, interference, and color substrate filters, depending on the filtering principles. As shown in Figure. S11a, although the filtering efficiency was highest in the quartz crystal filter, this filter limits the flexibility of the designed sensor. Flexible 650 nm and Flexible 550 nm are flexible, interference-type filters with cutoff wavelengths of 650 and 550 nm, respectively. The cellophane sheet is a flexible, color substrate filter that transmits light above and absorbs most visible light below 600 nm. Among the flexible filters, the cellophane was most effective in reducing the background light noise, which is mainly the light from the green OLED light source. All the optical filters presented in this study are commercially available. The crystal filter (FBH650-40, Thorlabs, Inc., USA) has a peak wavelength of 650 nm and full-width half maximum of 40 nm. The two kinds of flexible filters (Edmund Optics, Barrington, USA) and the cellophane can be purchased from any stationery store.

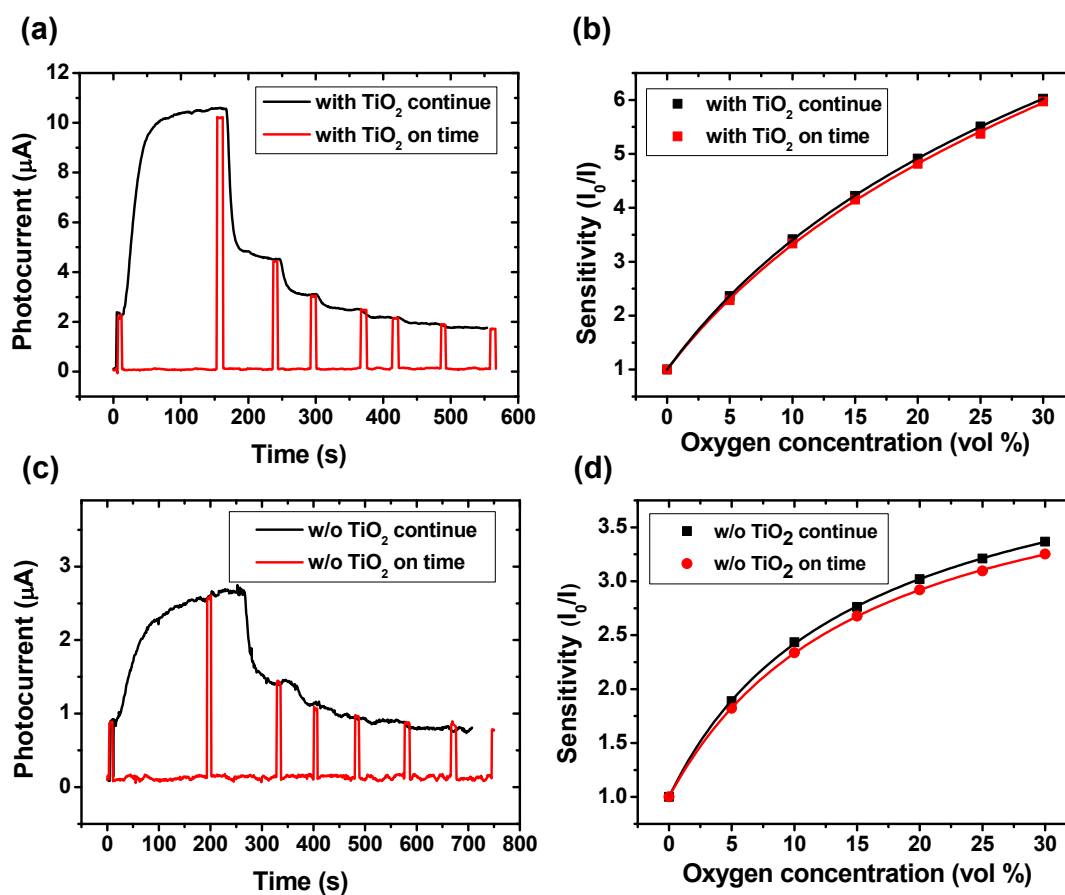


**Figure. S12** (a) Comparison between the photocurrent change for continuous and discrete measurements under varying  $[\text{O}_2]$  (0-30%, at every 5%) and the corresponding (b) SV plot of TiO<sub>2</sub> NP-doped sensing film. (c) Photocurrent change and (d) SV plot for the sensing film w/o TiO<sub>2</sub>.

For the continuous measurements, the Si-PD and LED were continuously in operation while the  $[\text{O}_2]$  was adjusted within the chamber via a mass flow controller. With experience, we could define the adjustment time for changing the  $[\text{O}_2]$ . The time that is needed for the adjustment of  $[\text{O}_2]$  within the chamber was 180, 90, and 60 s from the  $[\text{O}_2]$  in ambient air down to 0%, from 0% of  $[\text{O}_2]$  to 5%, and for every increase of 5% in  $[\text{O}_2]$  from then on, respectively. The LED light source was turned on for at least 6 s at a time. No significant difference was observed between the continuous and discrete measurements, as indicated by the data presented in Figure. S12.

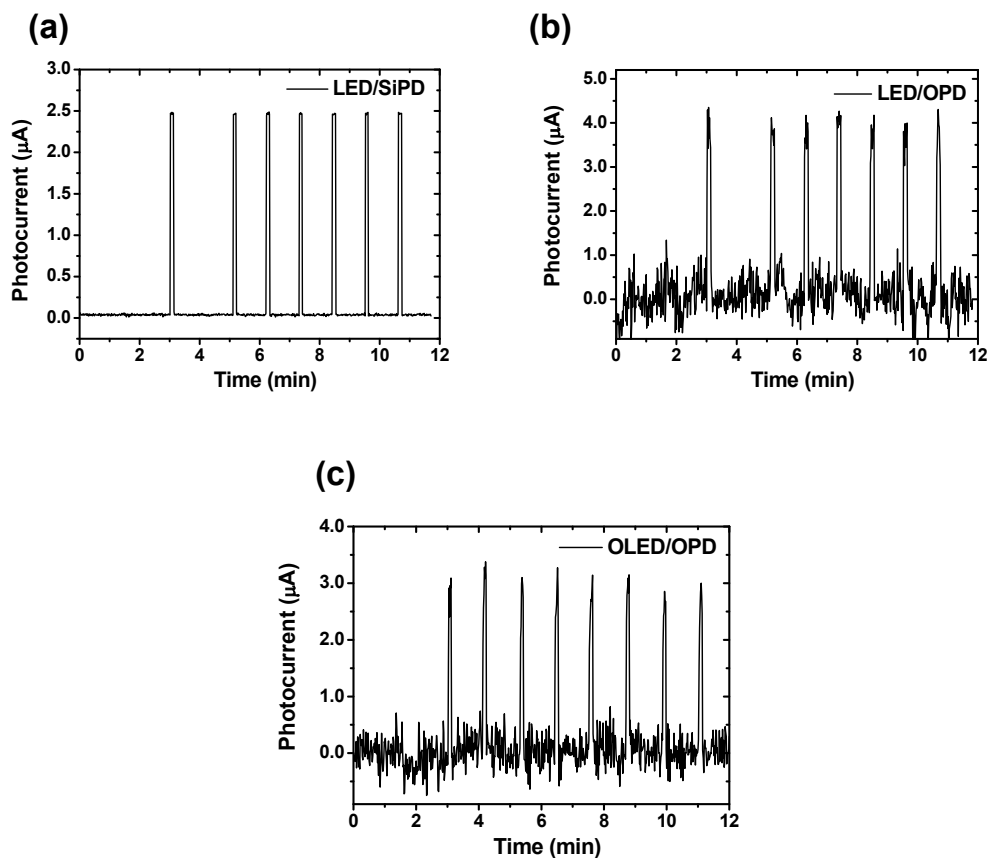


**Figure. S13** Degradation test results of the individual components of the integrated O<sub>2</sub> sensor. Sensing film PL-induced photocurrent was measured using illumination from the LED and detection by the (a) Si-PD, (b) OPD and (c) OLED illumination-induced OPD photocurrent.

The sensing degradation measurements of the TiO<sub>2</sub> NP-doped sensing film in Figure. S13a were performed using illumination from the LED and photon detection by the Si-PD. The sensing film PL-induced photocurrent was measured at time intervals of 180, 90, and 60 s. No degradation of the sensing film occurred during seven cycles of alternating (on-off) LED illumination. The degradation measurements of the OPD (Figure. S13b) were conducted using illumination from the LED. Compared with the baseline current noise, the detected

signal measured by the OPD shows stable operation of the device throughout the on-off illumination cycles (Figure. S13b). The degradation measurements of the OLEDs were measured using an OPD as the photodetector. The OPD photocurrent value presented in Figure. S13c was steadily decreasing due to the OLED degradation. When the photocurrent values were converted into  $O_2$  sensitivities, it was confirmed that the  $O_2$  sensitivity was 60% higher than the OPD or OLED degradation effects. Therefore, the  $[O_2]$  can be measured with our  $O_2$  sensing device despite the degradation of the OPD or OLED.

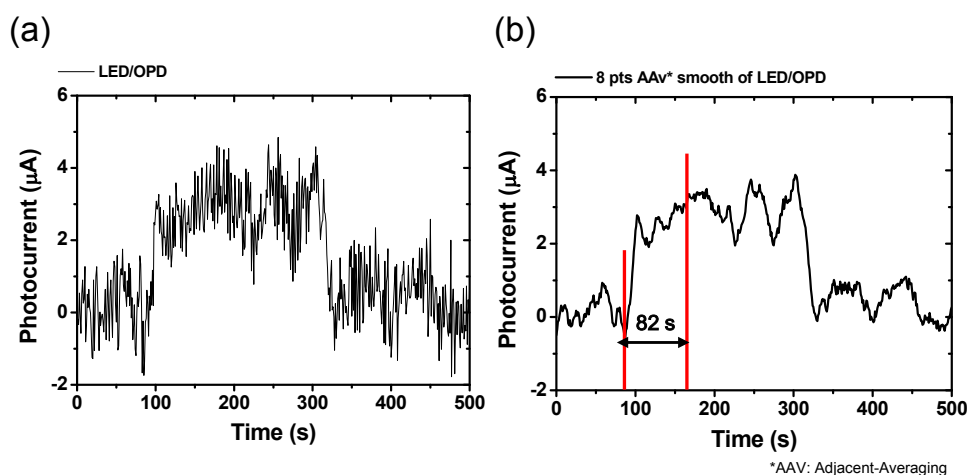


**Figure. S14.** Response time of the integrated  $O_2$  sensor. (a) Raw data of photocurrent detected by OPD with illumination from an LED (b) Smoothed data of photocurrent versus time graph.

Due to the degradation problem of OLED, the photocurrent was measured under illumination with a LED. The response time of the integrated sensor was 82 s when detected by OPD as shown in Figure. S14.

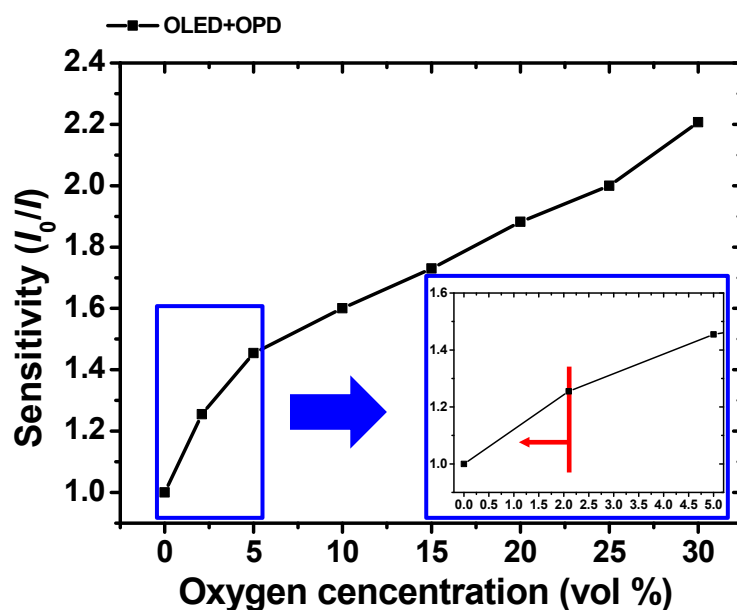


**Figure. S15.** The resolution of the O<sub>2</sub> sensing system. Inset in the graph indicates the resolution of the system is less than 2.1%.

For the measurement of resolution of the system, the OPD and OLED were operated while the [O<sub>2</sub>] was adjusted within the chamber via a mass flow controller. As shown in Figure. S15, it was confirmed that the sensitivity changes at an [O<sub>2</sub>] of 2.1% or less. In instrumental analysis for measurement of resolution of the sensing system, [O<sub>2</sub>] of 2.1% is the smallest value which can be controlled by mass flow controller.

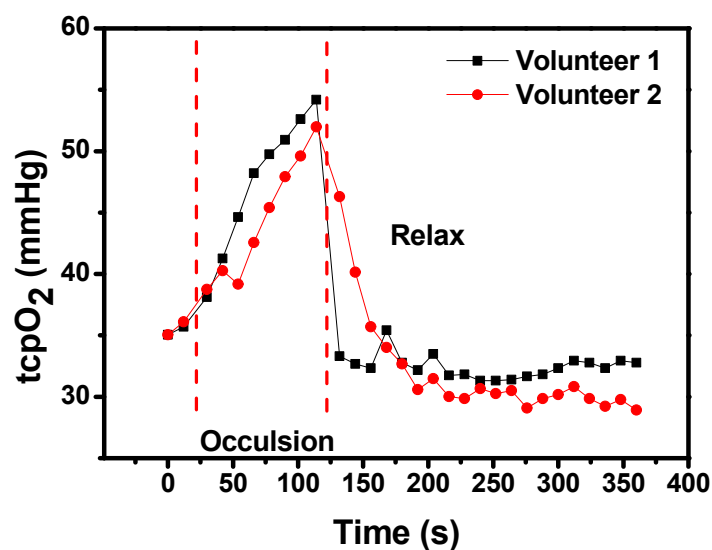


**Figure. S16.** The tcpO<sub>2</sub> variations of lower arm from two volunteers during 90 s of blood cuff restriction and 3 or 4 min of recovery measured by sensing film, LED and Si-PD.

## ABBREVIATIONS

IPA, isopropyl alcohol; ITO, Indium tin oxide; HTL, hole transport layer; ETL, electron transport layer; Cs<sub>2</sub>CO<sub>3</sub>, cesium carbonate

## REFERENCES

- (1) Gu, H.; Zhang, X.; Wei, H.; Huang, Y.; Wei, S.; Guo, Z. An overview of the magnetoresistance phenomenon in molecular systems. *Chem. Soc. Rev.* **2013**, 42 (13), 5907-5943.
- (2) Fujieda, I.; Ohta, M. Angle-resolved photoluminescence spectrum of a uniform phosphor layer. *AIP Adv.* **2017**, 7 (10), 105223, DOI: 10.1063/1.5000478.
- (3) Park, J. W.; Shin, D. C.; Park, S. H. Large-area OLED lightings and their applications. *Semicond. Sci. Technol.* **2011**, 26 (3), 034002.